Pseudospin topological phase transition induced by rotation operation in two-dimensional dielectric photonic crystal with C_6 symmetry

Wenjie Sui [a], Yu Zhang [a], Zirui Zhang [a], Hongfang Zhang [a,b,*], Qiang Shi [a,b], Zengtao Lv [a,b], Bing Yang [a,b,**]

[a] School of Physical Science and Information Engineering, Liaocheng University, Liaocheng 252059, China
[b] Shandong Provincial Key Laboratory of Optical Communication Science and Technology, Liaocheng 252059, China

ARTICLE INFO

ABSTRACT

We construct a kind of two-dimensional photonic crystal with triangular lattice in which the primitive cell contains six identical rods composed of two half cylinders with different dielectric materials. All the rods have the same rotations around themselves, ensuring that the system preserves the C_6 symmetry. The pseudospin topological phase transition (TPT) of the system is realized by rotating the rod elements, and the helical edge states (HESs) are constructed along the interface between two photonic crystals with opposite rotations. Numerical results and simulations reveal that the HESs are topologically protected with the pseudospin-locked unidirectional propagation of electromagnetic waves with robustness against corners and defects along the interface. Adjusting the size of rod elements, the TPT can be engineered at needed frequency.

1. Introduction

Topology is an important branch of mathematics, focusing on the invariants of a system under continuous variations of other parameters [1]. The discovery of the quantum Hall effect opens a new chapter in the study of condensed matter physics concerning the topological properties of a system [2]. Unidirectional propagation of topological edge state (TES) without backscattering can exist along the interface between structures with different topological properties. This kind of unidirectional transmission of energies is robust to imperfections along interface in the system due to the topological protection, which has potential applications in the future spintronics and quantum computing [3,4].

In 2005, Haldane et al. first introduced the concept of topology to the field of photonics [5]. They predicted that a kind of chiral edge state similar to that of the quantum Hall effect in electronics can be realized by breaking the time reversal symmetry (TRS) of electromagnetic (EM) wave when an external field is added along gyroelectric cylinders. However, this kind of photonic topological states (PTSs) is not observed in experiment due to the weak magneto-optical effect of gyroelectric materials. In 2008, Wang et al. proposed an alternative solution by using gyromagnetic cylinders instead of gyroelectric cylinders [6]. The next year, they experimentally observed such topologically protected PTSs for the first time [7]. Since then, constructing PTSs by breaking the TRS in magneto-optic materials has been a hot topic

in field of photonics [8–12]. However, due to the requirement of the external magnetic field and the limitation of magnetic response speed in magneto-optic material, the PTSs in magnetic material can only be realized in the microwave frequency range, and cannot be extended to the visible and infrared light area, which impedes them to integrate with current widely used optical communication and optical computing techniques. To this end, researchers have made attempts to seek and design other PTSs, such as the topological states with pseudospin protection in coupled ring waveguides [13], the Floquet PTSs in helical waveguide arrays [14–16], and pseudospin PTSs in bianisotropic metamaterials [17].

Among these PTSs, the pseudospin topological states proposed by Hu et al. in 2015 has attracted more attentions due to the full dielectric material design, simple structure, easy realization in visible and infrared frequencies, and friendly integration with current photonics technologies [18]. Their design was based on a two-dimensional (2D) triangular lattice photonic crystal containing six identical dielectric rods in each primitive cell. And each rod has the same distance from the center of the primitive cell. By shrinking or expanding the six rods structure in primitive cell through adjusting the distance between the rods and center of the primitive cell, frequency band structures of the photonic crystal can be engineered. By combining the TRS of EM wave with the C_{6v} symmetry of the lattice itself, they constructed the pseudo-TRS operation of the system. And by analogy with the p and d orbitals structure in electronic system, they designed the
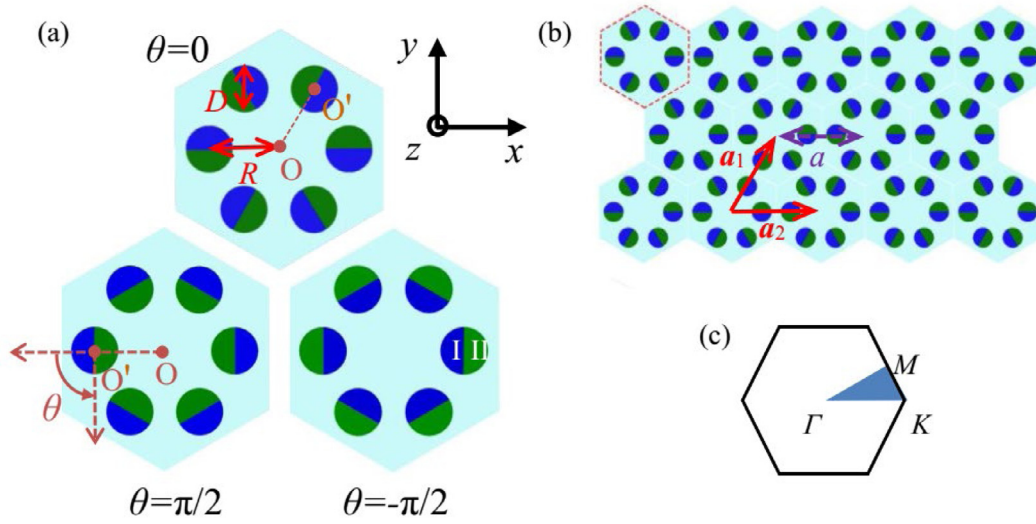

Fig. 1. (a) Primitive cells of the 2D triangular lattice photonic crystals. Upper panel, lower left and lower right panels are for the cases with $\theta = 0$, $\pi/2$ and $-\pi/2$, respectively; (b) Periodic structure of the photonic crystal; (c) First Brillouin zone of the periodic structure.

photonic pseudospin states p_+, p_-, d_+ and d_- of the transverse magnetic (TM) modes in the photonic crystal. Along the interface between two photonic crystals with different pseudospins, the helical edge states (HESs) with pseudospin-locked unidirectional propagation of EM wave can be constructed.

Recently, many pseudospin PTSs based on structures with C_{6v} symmetry have been proposed theoretically [19–21] and the unidirectional transmission of such pseudospin-locked HESs have also been observed experimentally, and some other photonic crystal structures [22–31] have also been proposed to construct the pseudospin PTSs through moving the scattering elements in the primitive cell. However, in these systems, accurately controlling the movement of rod elements is hard, and the moving is also constrained by the size of the primitive cell. So, in this paper, we design a kind of 2D triangular lattice photonic crystal with its primitive cell containing six identical rods composed of two half cylinders with different dielectric materials. Only by rotating each rod in the system, the p and d orbitals can be exchanged, and the pseudospin topological phase transitions (TPTs) are realized and the HESs are constructed. Our design is simple to operate and easy to implement, and our scheme also avoids the geometric constraints of moving of the rods in the system during the regulation of the PTSs.

2. Models and pseudospin TPTs

Our model is a 2D triangular lattice photonic crystal containing six identical rods in a primitive cell with each rod made of two half cylinders with different dielectric materials. Figs. 1(a) and 1(b) show the schematic plots of the primitive cell and the periodic structure of the photonic crystal, respectively, with a_1 and a_2 the lattice vectors and a the lattice constant. The circles in the figure are dielectric rods with blue semicircle and green semicircle denoting material I and material II, respectively. The background area is air. The diameter of the rods is D, and the distance between center of the primitive cell (O) and center of each dielectric rod (O') is R. Each rod has the same rotation angle θ around its own center O'. The upper panel in Fig. 1(a) shows the primitive cell of the photonic crystal at $\theta = 0$, with the boundary between two semicircles in each rod collinear with the line through O and O'. The lower left and lower right panels in Fig. 1(a) show the primitive cells of $\theta = \pi/2$ and $-\pi/2$, respectively, with the counterclockwise being the positive rotation direction. Clearly, for a particular rotation angle θ, the structure has the C_6 symmetry. Fig. 1(c) shows the first Brillouin zone of the system.

In our studies, we take the relative permittivity of material I and material II as $\varepsilon_1 = 11.7$ and $\varepsilon_2 = 3.9$, respectively, and the relative permittivity of air as $\varepsilon_A = 1$. The relative permeability of all the components is $\mu_r = 1$. By taking values of $R = 0.3327a$ and $D = 0.22a$ (A doubly degenerate Dirac point can be formed at point Γ in the Brillouin zone at case of $\theta = 0$), we show the frequency band structures for the cases of $\theta = -\pi/2$, 0 and $\pi/2$, respectively, in Fig. 2(a)–2(c). Here, $\omega a/2\pi c$ is the reduced frequency with ω the angular frequency and c the speed of light in vacuum. The numbers in Fig. 2(a) label the frequency bands from low to high, and $M_{(4)}$ represents the symmetry point M of the fourth band in the first Brillouin zone. The insets in the left and in the right of Fig. 2(d) show the two pairs of orthogonal bases of the electric field mode $|E_z|$ at the doubly degenerate points of the frequency band at point Γ in Figs. 2(a) and 2(c), respectively, where the dipole and quadruple states of p orbitals (p_x, p_y) and d orbitals (d_{xy}, $d_{x^2+y^2}$) can be recognized clearly.

As can be seen from Fig. 2(a) at $\theta = -\pi/2$, the frequency of p orbital (degeneracy of the 2th and 3th bands) is lower than d orbital (degeneracy of the 4th and 5th bands), and the opened band gap is topological trivial denoted with cyan. As $\theta = 0$ in Fig. 2(b), the p orbital and d orbital degenerate together, corresponding to the double Dirac cones (degeneracy of the 2th–5th bands). As $\theta = \pi/2$ in Fig. 2(c), the d orbital (degeneracy of the 2th and 3th bands) is lower than p orbital (degeneracy of the 4th and 5th bands), the opened band gap is topologically nontrivial highlighted with green. Obviously, the band inversion occurs when the rotation angle θ changes from $\theta = -\pi/2$ in Fig. 1(a) to $\theta = \pi/2$ in Fig. 1(c), and therefore the pseudospin TPT is realized [32]. Fig. 2(d) shows the detailed results of the opened band gap with variations of the rotation angle θ of the rods. Here, due to the symmetry of the system, we only give out results within the range of $-\pi/2 \leq \theta \leq \pi/2$. As can be seen from Fig. 2(d), when $\theta < 0$, the opened band gap highlighted with cyan is trivial, and when $\theta > 0$ the opened band gap highlighted with green is topologically nontrivial. The widths of the band gaps increase with the increase of rotation angle $|\theta|$. When the rotation angles in both clockwise and counterclockwise directions take the same values of $|\theta|$, the widths of band gaps get almost the same values, which facilitate the construction and regulation of the HESs with our model. It is worth noting that as $|\theta|$ increases to about $|\theta| = \pi/3$, the frequency of d (p) orbital is higher than the frequency at $M_{(4)}$ (black line). At this time, the complete band gaps are defined within the frequency range between p (d) orbital and $M_{(4)}$ in counterclockwise (clockwise) rotations.
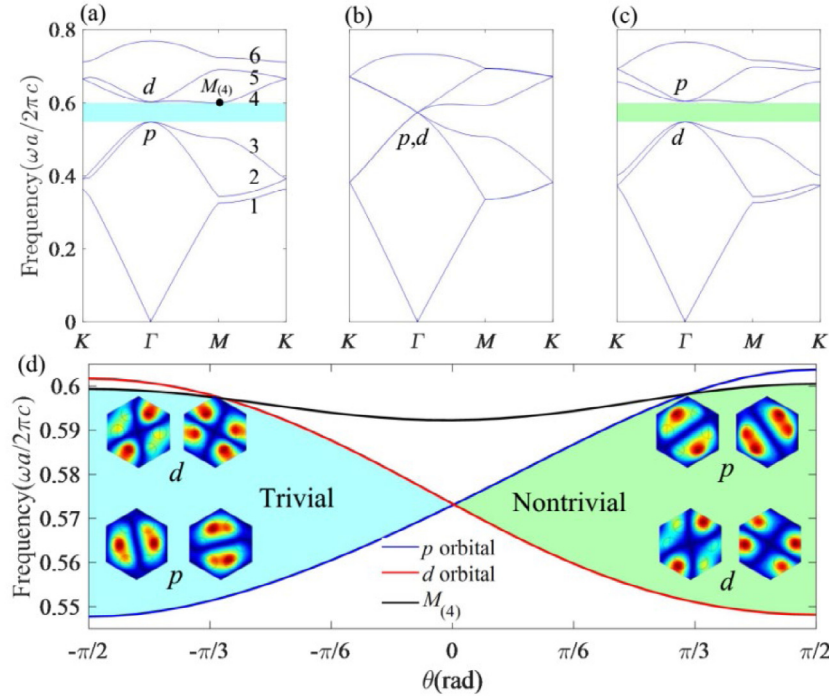
Fig. 2. Variations of frequency band structure with changes of rotation angle θ. (a)–(c) Band structures of the photonic crystal at $\theta = -\pi/2$, 0 and $\pi/2$, respectively; (d) Detailed results of the band gap with changes of rotation angle θ. Inserts in the left and the right show the distributions of field mode $|E_z|$ of p and d orbitals at point Γ in (a) and (c), respectively.

3. HESs and the unidirectional propagation

3.1. Construction of the HESs

If the two photonic crystals have different pseudospins within the frequency range of their common band gaps, there will be topologically protected HESs along the interface between them [33]. Here, we investigate the HESs along the zigzag edge between the two kinds of above photonic crystals with $\theta<0$ and $\theta>0$. For convenience, we mark the photonic crystal with $\theta>0$ as structure N, and the photonic crystal with $\theta<0$ as structure T in the following studies. The supercell of our model is shown in Fig. 3(a), in which the purple line indicates the zigzag interface. N is above the interface and T is in below. The supercell is arranged periodically in x direction, forming our simulation structure. Without loss of generality, in our studies, we only investigate the HESs constructed by N and T with the same rotation angles $|\theta|$. Fig. 3(b)–3(d) show the projection band diagrams along x direction for the cases of $|\theta| = \pi/8$, $\pi/4$ and $\pi/2$ in N and T, respectively. The gray areas denote the bulk states, and the red curves are the HESs.

From Fig. 3(b)–3(d), we can see that the band gap between the upper and lower body states enlarges as $|\theta|$ increases, which is due to the broadening of the common band gap in N and T as $|\theta|$ increases as shown in Fig. 2(d). It can also be seen that there is a gap in the HESs at point Γ, which makes the HESs split into two branches. This band gap comes from the breakdown of the C_6 symmetry at the interface of N and T. When $|\theta|$ is small, the C_6 symmetry is affected little, and the gap is very small. As $|\theta|$ increases to a large value, the C_6 symmetry at the interface is broken significantly, leading to a wide band gap between the two branches as shown in Fig. 3(d).

Fig. 3(e) shows the distributions of electric field mode $|E_z|$ and energy flow (Pointing vector S) of the two HESs with TRS marked with E and F in Fig. 3(d) at the frequency of $\omega a/2\pi c = 0.555$. From the $|E_z|$ distributions, we can clearly see that the fields are completely localized near the interface area between N and T. And from the distributions of S, it can be seen the counterclockwise and clockwise characteristics of

the energy flows of the edge states, corresponding to the pseudospin-up and pseudospin-down states at E and F, respectively. In addition, the left and the right transmissions of S at E and F clearly indicate the pseudospin-locked unidirectional propagation of the HESs. Due to the protection of the TRS, the two edge states with opposite pseudospins at E and F are orthogonal to each other, so the backscattering between them is suppressed and the pseudospin-locked EM waves with opposite propagations along the interface can be stimulated by the source with different pseudospins.

Fig. 3(f) and Fig. 3(g) show the simulation results of the propagation of EM wave ($|E_z|$) stimulated by pseudospin-up and pseudospin-down light sources at frequency of $\omega a/2\pi c = 0.555$ along the interface between N and T, corresponding to the edge states at E and F in Fig. 3(d). In our simulations, both N ($\theta = \pi/2$) and T ($\theta = -\pi/2$) structures are set to contain 14 primitive cells in y direction. The pseudospin point sources are denoted by yellow split rings with arrows representing their pseudospins at the interface. The point sources in Figs. 3(f) and 3(g) are set as $S_- = H_0 e^{i\omega t}(\hat{x} - i\hat{y})$ and $S_+ = H_0 e^{i\omega t}(\hat{x} + i\hat{y})$ with H_0 the magnetic field intensity, corresponding to the pseudospin-up of E and pseudospin-down of F in Fig. 3(d), respectively. Clearly, the EM waves stimulated by S_- and S_+ propagate in the $+x$ and $-x$ directions, respectively, demonstrating the pseudospin-locked unidirectional propagation of the HESs.

3.2. Unidirectional propagation of the HESs

To investigate the unidirectional propagation of the HESs constructed above, we calculate the propagation of EM waves stimulated by pseudospin sources along the interface between N and T as rotation angle $|\theta|$ takes different values. In the simulation model as shown in Fig. 3(g), we calculate the time averaged energy density w_A and w_B through two cut lines denoted by A and B (dotted lines in the figure) [34]. Here, both A and B are $8a$ ($4a$ in each of N and T) in y direction and $15a$ away from the source along the interface.
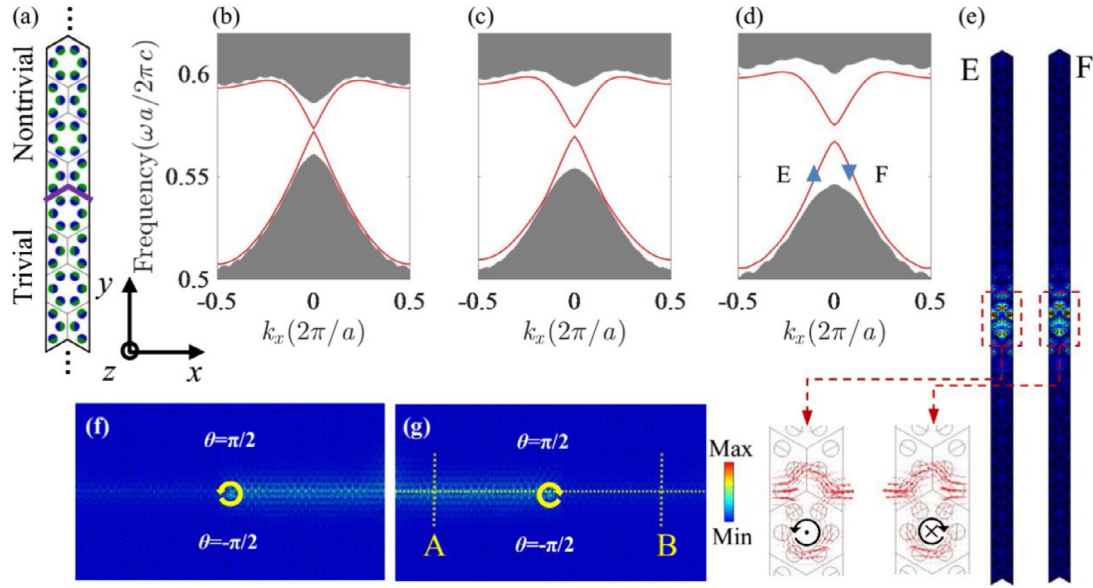
Fig. 3. (a) Supercell for calculation of projected diagram; (b)–(d) Projected diagram of edge states at interface of two photonic crystals with different pseudospins when $|\theta| = \pi/8$, $\pi/4$ and $\pi/2$, respectively. Shaded areas are bulk states, and red curves are HESs; (e) Distributions of electric field mode $|E_z|$ and Pointing vector S at HESs of E and F. (f), (g) Simulation results of the propagation of EM wave ($|E_z|$) stimulated by sources at frequency of $\omega a/2\pi c = 0.555$ along the interface between N ($\theta = \pi/2$) and T ($\theta = -\pi/2$), corresponding to the HESs at E and F. Point sources are denoted by yellow split rings with the arrow representing the pseudospin.
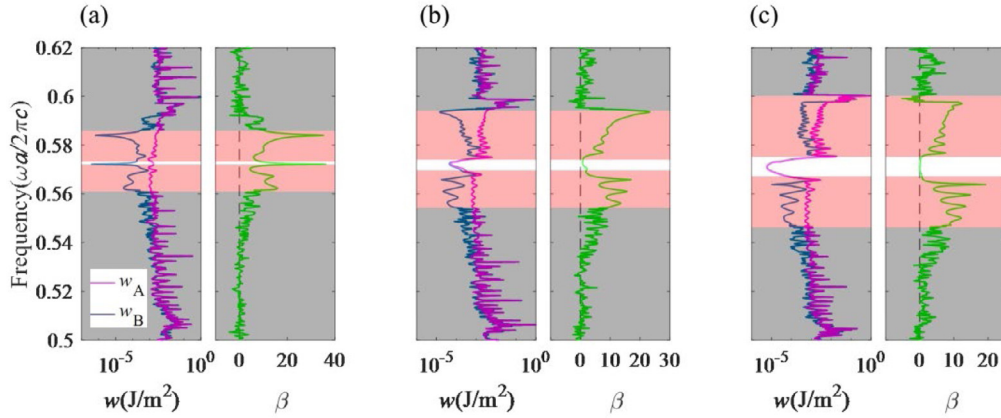

Fig. 4. Unidirectional propagation of the EM waves stimulated by pseudospin sources along the interface between N and T as rotation angle takes values of $|\theta| = \pi/8$, $\pi/4$ and $\pi/2$ in (a)–(c), respectively.

Also, we calculate the unidirectional isolation rate to characterize the unidirectional property of the HESs with

$$\beta = 10 \times \lg \frac{w_A}{w_B}$$

The results for the cases of $|\theta| = \pi/8$, $\pi/4$ and $\pi/2$ are shown in Fig. 4(a)–4(c), with the magenta lines and blue lines denoting the w_A and w_B, and the green lines denoting the unidirectional isolation rate β, respectively. The red background in the figure marks the frequency range where the HESs are located, and the white background marks the frequency range where the band gaps between two branches of the HESs are located. The gray background denotes the frequency range where the body states are located.

It can be seen that as $|\theta|$ takes different values, both the upper and the lower branches of the HESs support well unidirectional transmission of the EM waves with the unidirectional isolation rate β almost greater than 10 dB, indicating that the pseudospin-locked EM wave propagation to the left is much larger than those to the right. At the case of $|\theta| = \pi/8$, due to the fact that the band gap between two branches of the HESs is very narrow, the confinement of the band gap on the leftward

propagation (w_A) of the EM wave is quite weak, so the pseudospin-locked EM wave within the tiny gap can still achieve large values of β. As $|\theta|$ increases, the band gap is broadened, and its suppression on the propagation of EM waves appears, resulting in the significant decrease of both w_A and w_B, and near zero value of β correspondingly within the frequency range of the band gap. Clearly, within the frequency range of the bulk state, the EM waves have no unidirectional propagation at all. It is worth noting that at $|\theta| = \pi/2$, the EM wave at frequencies around $\omega a/2\pi c = 0.6$ within the upper branch of HESs cannot achieve unidirectional transmission, which is due to the nearly flat structure of the upper edge state here as shown in Fig. 3(d).

3.3. Robustness of the unidirectional propagation of the HESs

The pseudospin-locked unidirectional propagation of the HESs are topologically protected with robustness against imperfections along the interface. In Fig. 5(a)–5(d), we design a "U" type edge containing both 120° and 60° corners. The upper part of the interface is structure N and the lower part is structure T with $|\theta| = \pi/2$. Point sources with different pseudospins denoted by yellow split rings with arrow at
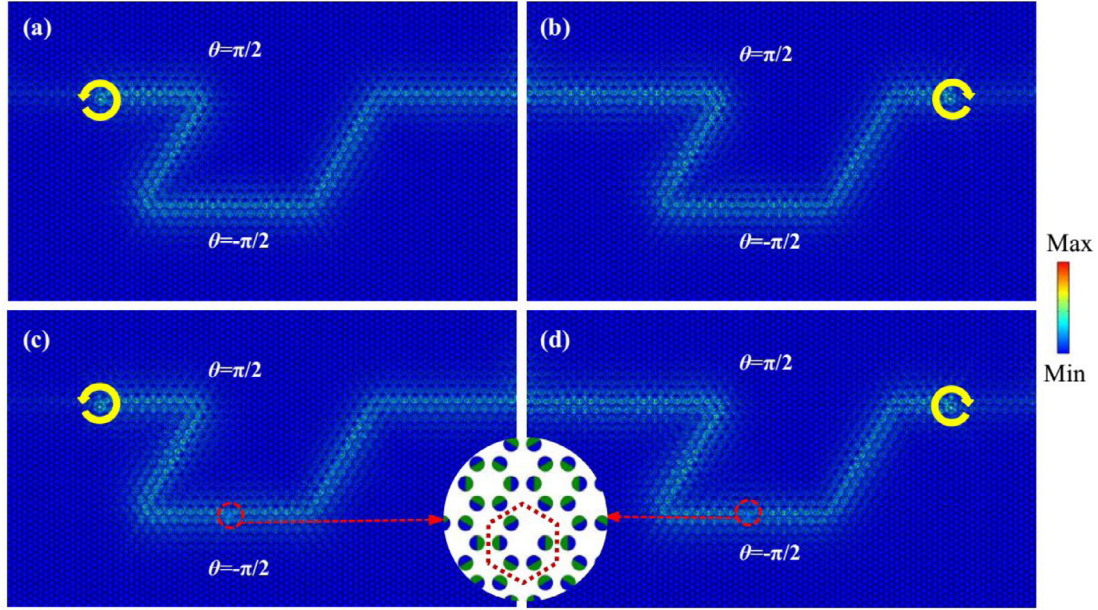
Fig. 5. Simulations of the robustness of the HESs. (a), (b) Unidirectional propagation of EM waves stimulated by pseudospin-up and pseudospin-down sources, respectively, along a "*U*" type edge containing both 120° and 60° corners. (c), (d) A rod is removed from the interface to form a defect (enlarged in the inset).
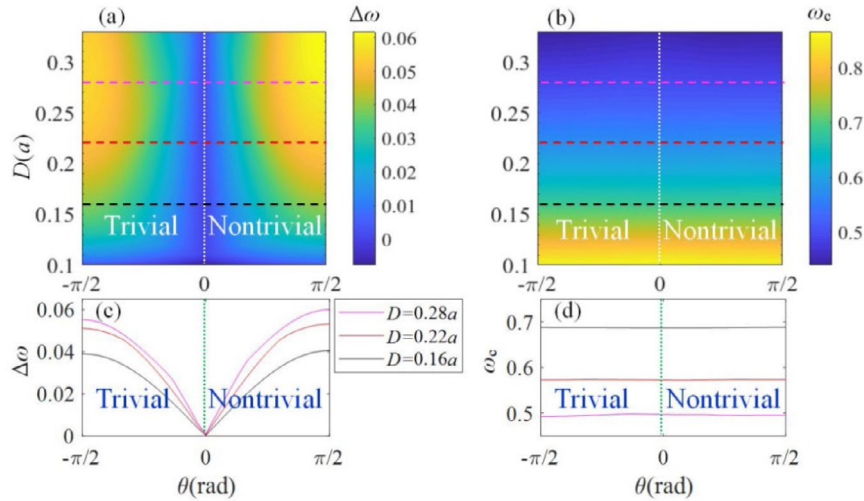

Fig. 6. (a), (b) Widths and positions of the band gaps with changes of the rotation angle θ and diameter D of the rods, respectively. The magenta, red and black dashed lines denote the cases of $D = 0.28a$, $0.22a$ and $0.16a$, respectively. (c), (d) $\Delta\omega - \theta$ and $\omega_c - \theta$ curves at $D = 0.28a$, $0.22a$ and $0.16a$, respectively.

frequency of $\omega a/2\pi c = 0.555$ are used to stimulate the HESs. The results in Figs. 5(a) and 5(b) show that the pseudospin-locked unidirectional propagation of EM waves can bypass the sharp corners with almost no backscattering loss. Moreover, in Figs. 5(c) and 5(d), a rod is removed from the interface to form a defect in red dotted circle (enlarged in the inset). It can be seen that the EM waves can still bypass the defects and corners with almost no loss. So the unidirectional propagation of the HESs constructed in the models is robust against the imperfections along the edge.

3.4. Effect of size of rods on the TPTs

The above research fixes the diameter of the rod in photonic crystal, and the TPTs are realized by rotating the rod elements. The widths of the topological band gaps can be changed by adjusting the rotation angle. In addition, the TPTs can also be engineered by changing size of the rods in photonic crystal. Based on the above research, by setting

the lowest frequency of the band above the band gap with ω_t, and the highest frequency of the band below the band gap with ω_b, we define the reduced frequency width of the complete band gap as $\Delta\omega = (\omega_t - \omega_b)a/2\pi c$ and the reduced frequency center of the band gap as $\omega_c = (\omega_t + \omega_b)a/2\pi c$. Figs. 6(a) and 6(b) show the changes of $\Delta\omega$ and ω_c as D and θ vary, respectively. Here, the value of R is taken around $a/3$, ensuing that at the case of $\theta = 0$, the width of band gap is zero, corresponding to the double degenerate Dirac point at Γ point in the Brillouin zone. It is worth noting that since the structure here only has C_6 symmetry, the double degenerate Dirac point appears near $R = a/3$, not exactly at $R = a/3$ (| R-$a/3$| <0.001a). In Figs. 6(c) and 6(d), we show the $\Delta\omega - \theta$ and $\omega_c - \theta$ curves at three particular values of D at $D = 0.16a$, $0.22a$ and $0.28a$, corresponding to the magenta, red and black dashed lines in Figs. 6(a) and 6(b), respectively.

As can be seen from Fig. 6(a), starting from $\theta = 0$, both clockwise ($\theta<0$) and counterclockwise ($\theta>0$) rotation of the rod elements can open the double degenerate Dirac point and lift band gaps. The band

gaps with $\theta<0$ are topologically trivial and those with $\theta>0$ are topologically nontrivial. The widths of the band gaps increase with increase of the rotation angle $|\theta|$. The opening of the band gaps are also related to the rod sizes. For example, the maximum width of the band gap at $\theta = \pi/2$ enlarges with increases of D, which can also be seen in Fig. 6(c). From Figs. 6(b) and 6(d), we can find that with increases of the rod sizes, the center of the band gap ω_c is gradually decreased, and the rotation angle θ almost has no effect on it. The decrease of the ω_c is due to the enlargement of the duty factor of the system as the size of rod elements increases [35]. Rotations of the rods introduce no changes of the duty factor of the structure which ensures the constant values of ω_c at particular rod sizes. The variation characteristics of the bad gaps with the sizes and rotation angles of rod elements in photonic crystals facilitate us to engineer the TPTs in these structures.

4. Conclusions

We construct a 2D triangular lattice photonic crystal with the C_6 symmetry. The scattering rods are made of two half cylinders with different dielectric constants. Through rotating the rod elements around their centers, we realize the band inversions and the pseudospin TPTs of the system. The pseudospin-locked HESs with topological protection are designed along the interfaces between two photonic crystals with opposite rotation angle of the rods. The HESs support the unidirectional propagation of the pseudospin-locked EM waves with immune to the imperfections along the edges. By changing sizes of the rod elements, the TPTs can be adjusted within the needed frequency range. In practice, the two half cylinders forming the rod can be bonded by gel. The gel thickness can be neglected, which does not affect the properties of the rod. Also the rod is of finite length (wavelength order) in realization, so the two half cylinders can also be held together by an external ring at each end of the rod. Our proposal provides an optional way to construct the photonic pseudospin topological phases, and our design is simple and easy to realize in practice.

Declaration of competing interest

The authors declare that they have no known competing financial interests or personal relationships that could have appeared to influence the work reported in this paper.

Data availability

Data will be made available on request.

Acknowledgments

References

[1] L. Lu, J.D. Joannopoulos, M. Soljačić, Topological photonics, Nat. Photonics 8 (11) (2014) 821–829.
[2] M.Z. Hasan, C.L. Kane, Colloquium: Topological insulators, Rev. Modern Phys. 82 (4) (2010) 3045–3067.
[3] Y. Wu, C. Li, X. Hu, Y. Ao, Y. Zhao, Q. Gong, Applications of topological photonics in integrated photonic devices, Adv. Opt. Mater. 5 (18) (2017) 1700357.
[4] T. Ozawa, H.M. Price, A. Amo, N. Goldman, M. Hafezi, L. Lu, M.C. Rechtsman, D. Schuster, J. Simon, O. Zilberberg, I. Carusotto, Topological photonics, Rev. Modern Phys. 91 (1) (2019) 015006.
[5] F.D. Haldane, S. Raghu, Possible realization of directional optical waveguides in photonic crystals with broken time-reversal symmetry, Phys. Rev. Lett. 100 (1) (2008) 013904.
[6] Z. Wang, Y.D. Chong, J.D. Joannopoulos, M. Soljacic, Reflection-free one-way edge modes in a gyromagnetic photonic crystal, Phys. Rev. Lett. 100 (1) (2008) 013905.
[7] Z. Wang, Y. Chong, J.D. Joannopoulos, M. Soljacic, Observation of unidirectional backscattering-immune topological electromagnetic states, Nature 461 (7265) (2009) 772–775.
[8] H.-C. Chan, G.-Y. Guo, Tuning topological phase transitions in hexagonal photonic lattices made of triangular rods, Phys. Rev. B 97 (4) (2018) 045422.
[9] Y. Poo, R.X. Wu, Z. Lin, Y. Yang, C.T. Chan, Experimental realization of self-guiding unidirectional electromagnetic edge states, Phys. Rev. Lett. 106 (9) (2011) 093903.
[10] H. Zhang, W. Sui, Y. Zhang, G. Liu, Q. Shi, Z. Lv, D. Zhang, C. Rong, B. Yang, Disorder-driven collapse of topological phases in photonic topological insulator, Phys. Status Solidi B 2200214, http://dx.doi.org/10.1002/pssb.202200214.
[11] B. Yang, T. Wu, X. Zhang, Engineering topological edge states in two dimensional magnetic photonic crystal, Appl. Phys. Lett. 110 (2) (2017) 021109.
[12] B. Yang, H. Zhang, T. Wu, R. Dong, X. Yan, X. Zhang, Topological states in amorphous magnetic photonic lattices, Phys. Rev. B 99 (4) (2019) 045307.
[13] M. Hafezi, S. Mittal, J. Fan, A. Migdall, J.M. Taylor, Imaging topological edge states in silicon photonics, Nat. Photonics 7 (12) (2013) 1001–1005.
[14] M.C. Rechtsman, J.M. Zeuner, Y. Plotnik, Y. Lumer, D. Podolsky, F. Dreisow, S. Nolte, M. Segev, A. Szameit, Photonic floquet topological insulators, Nature 496 (7444) (2013) 196–200.
[15] S. Mukherjee, A. Spracklen, M. Valiente, E. Andersson, P. Ohberg, N. Goldman, R.R. Thomson, Experimental observation of anomalous topological edge modes in a slowly driven photonic lattice, Nat. Commun. 8 (1) (2017) 13918.
[16] L.J. Maczewsky, J.M. Zeuner, S. Nolte, A. Szameit, Observation of photonic anomalous floquet topological insulators, Nat. Commun. 8 (1) (2017) 13756.
[17] W.J. Chen, S.J. Jiang, X.D. Chen, B. Zhu, L. Zhou, J.W. Dong, C.T. Chan, Experimental realization of photonic topological insulator in a uniaxial metacrystal waveguide, Nat. Commun. 5 (1) (2014) 5782.
[18] L.H. Wu, X. Hu, Scheme for achieving a topological photonic crystal by using dielectric material, Phys. Rev. Lett. 114 (22) (2015) 223901.
[19] Y.-F. Gao, M.-C. Jin, Q. Zhou, Q.-C. Hou, J.-P. Sun, H. Song, B.-W. Shen, Non-spin-mixing defect modes in the split-ring dielectric photonic crystals, Opt. Commun. 492 (2021) 126963.
[20] X. Xu, J. Huang, H. Zhang, X. Guo, S. Mu, Y. Liu, N. Zhai, Topological transition and topological line defects in dielectric photonic crystals, Opt. Commun. 498 (2021) 127262.
[21] B. Yan, J. Xie, E. Liu, Y. Peng, R. Ge, J. Liu, S. Wen, Topological edge state in the two-dimensional stampfli-triangle photonic crystals, Phys. Rev. Appl. 12 (4) (2019) 044004.
[22] Y. Fang, Z. Wang, Highly confined topological edge states from two simple triangular lattices with reversed materials, Opt. Commun. 479 (2021) 126451.
[23] W.-J. Sui, Y. Zhang, Z.-R. Zhang, X.-L. Wang, H.-F. Zhang, Q. Shi, B. Yang, Study on unidirectional propagation control of helical edge states in topological spin photonic crystals, Acta Phys. Sin http://dx.doi.org/10.7498/aps.71.20220353.
[24] H. Huang, S. Huo, J. Chen, Reconfigurable topological phases in two-dimensional dielectric photonic crystals, Crystals 9 (4) (2019) 221.
[25] M.-C. Jin, Y.-F. Gao, Q.-L. Ma, W. Zhang, H. Song, J.-P. Sun, Regularly multiple double Dirac cones in photonic bands and topological transitions of all-dielectric photonic crystals, Phys. Rev. Mater. 5 (2) (2021) 024204.
[26] Z. Li, H.-C. Chan, Y. Xiang, Fragile topology based helical edge states in two-dimensional moon-shaped photonic crystals, Phys. Rev. B 102 (24) (2020) 245149.
[27] J. Ma, X. Li, Y. Fang, Embedded topological edge states from reversed two-dimensional photonic crystals, Physica E 127 (2021) 114517.
[28] J. Ma, C. Ouyang, L. Niu, Q. Wang, J. Zhao, Y. Liu, L. Liu, Q. Xu, Y. Li, J. Gu, Z. Tian, J. Han, W. Zhang, Topological edge state bandwidth tuned by multiple parameters in two-dimensional terahertz photonic crystals with metallic cross structures, Opt. Express 29 (20) (2021) 32105–32113.
[29] H.-X. Wang, H. Chen, J.-H. Jiang, G.-Y. Guo, Tunable edge states in reconfigurable photonic crystals, J. Appl. Phys. 126 (19) (2019) 193105.
[30] X.-X. Wang, X. Hu, Reconfigurable topological waveguide based on honeycomb lattice of dielectric cuboids, Nanophotonics 9 (10) (2020) 3451–3458.
[31] L. Xu, H.X. Wang, Y.D. Xu, H.Y. Chen, J.H. Jiang, Accidental degeneracy in photonic bands and topological phase transitions in two-dimensional core–shell dielectric photonic crystals, Opt. Express 24 (16) (2016) 18059–18071.
[32] S.J. Palmer, V. Giannini, Berry bands and pseudo-spin of topological photonic phases, Phys. Rev. Res. 3 (2) (2021) L022013.
[33] Z. Wen, S. Zeng, D. Wang, Y. Jin, B. Djafari-Rouhani, Robust edge states of subwavelength chiral phononic plates, Extrem. Mech. Lett. 44 (2021) 101209.
[34] B. Yang, H. Zhang, Q. Shi, T. Wu, Y. Ma, Z. Lv, X. Xiao, R. Dong, X. Yan, X. Zhang, Details of the topological state transition induced by gradually increased disorder in photonic Chern insulators, Opt. Express 28 (21) (2020) 31487–31498.
[35] J.D. Joannopoulos, S.G. Johnson, J.N. Winn, R.D. Meade, Photonic Crystals: Molding The Flow of Light, second ed., Princeton University Press, New Jersey, 2008.